

Article

Electrochemical Behavior of Natural Manganese Oxides: Transforming Mining Waste into Energy Storage Materials

George Soulamidis ^{1,*}, Maria Kourmoussi ^{2,3} , Christiana A. Mitsopoulou ^{2,3}  and Christina Stouraiti ¹ 

¹ Department of Geology and Geoenvironment, National and Kapodistrian University of Athens, Panepistimiopolis, 15784 Athens, Greece; chstouraiti@geol.uoa.gr

² Department of Chemistry, National and Kapodistrian University of Athens, Panepistimiopolis, 15771 Athens, Greece; marokourm@chem.uoa.gr (M.K.); cmitsop@chem.uoa.gr (C.A.M.)

³ Research Institute of Energy-Renewable Sources and Transport, University Center of Research 'Antonis Papadakis', National and Kapodistrian University of Athens, Panepistimiopolis, 15771 Athens, Greece

* Correspondence: gsoulamidis@geol.uoa.gr

Abstract: The present research explores the potential of manganese oxide waste ore in energy storage applications, focusing on supercapacitors. The investigation assesses the electrochemical capabilities of natural manganese oxides obtained from the Drama region, which has been the main mining center of Greece for manganese ore, especially that of battery-grade quality. Samples were collected from abandoned mining sites in the Kato Nevrokopi area, Drama. The structure and composition of the manganese minerals were determined by X-ray diffraction (XRD) and transmission electron microscopy (TEM). Electrochemical tests involved the preparation of electrodes using natural nsutite and heat-treated nsutite (hausmannite). Then, the designed electrodes were subjected to cyclic voltammetry tests and charge–discharge measurements. The hausmannite electrode exhibited a higher specific capacitance of 667 F/g at a current density of 0.2 A/g, and the electrode material retained 98.3% of its initial capacitance after 1000 cycles. This study provides new perspectives on simple and efficient methods for transforming natural nsutite material from mining waste to hausmannite with greater structural homogeneity and better electrochemical behavior.

Keywords: manganese oxides; mining waste; reuse; nsutite; hausmannite; energy storage



Citation: Soulamidis, G.; Kourmoussi, M.; Mitsopoulou, C.A.; Stouraiti, C. Electrochemical Behavior of Natural Manganese Oxides: Transforming Mining Waste into Energy Storage Materials. *Minerals* **2024**, *14*, 455. <https://doi.org/10.3390/min14050455>

Academic Editors: Anthimos Xenidis, Konstantinos Komnitsas, Vasilios Melfos and Ilhwan Park

Received: 21 February 2024

Revised: 18 April 2024

Accepted: 24 April 2024

Published: 26 April 2024



Copyright: © 2024 by the authors. Licensee MDPI, Basel, Switzerland. This article is an open access article distributed under the terms and conditions of the Creative Commons Attribution (CC BY) license (<https://creativecommons.org/licenses/by/4.0/>).

1. Introduction

Manganese oxides (Mn_xO_y) are renowned for their diverse range of niche applications in energy production and wastewater treatment [1]. These applications include heavy metal adsorption [2,3], serving as inorganic catalysts for oxygen reactions [4], and playing a crucial role in energy storage applications, notably in rechargeable lithium batteries [5]. More specifically, electrochemical-based storage devices such as batteries, capacitors, and supercapacitors provide a clean, low-cost, sustainable energy conversion and storage for renewable energy sources [6].

Identifying manganese oxide minerals poses a challenge due to their nano-crystalline nature, complex intergrowth of different phases, and structural and oxidation-state variations (Mn^{2+} to Mn^{7+}) [7]. The atomic frameworks of these minerals are constructed from Mn-O octahedra that share edges and link corners to yield an array of phases with tunnel or layer structures [8,9]. The tunnel-structured Mn oxides are assembled from single, double, or even triple chains of edge-sharing MnO_6 octahedra, and the chains share corners to manufacture frameworks that consist of tunnels with square or rectangular cross-sections. In contrast, the layer-structured Mn oxides comprise stacks of sheets of edge-sharing MnO_6 octahedra [7–9].

Manganese oxides have several crystallographic polymorphs. γ - MnO_2 is the synthetic analog of the mineral nsutite, and both of them are among the most critical manganese dioxides due to their application as an electrode material for the battery industry [10,11]. It

consists of an intergrowth structure of β - MnO_2 type tunnels (1×1) and ramsdellite- MnO_2 type tunnels (2×1), first described by De Wolff in 1959 [12]. Later, in 1995, Chabre and Pannetier proposed an additional structural defect, aside from the De Wolff defect, which is called micro-twinning and is accountable for the poor quality of X-ray powder diffraction patterns of most γ - MnO_2 and is correlated to the structure with their use as battery-grade material [13].

The development of manganese oxide materials for storing and converting energy has become increasingly important, prompting extensive research efforts. MnO_2 is particularly attractive in the battery sector due to its high theoretical capacitance, affordability, and low toxicity. Since its inception as a depolarizing agent in zinc alkaline cells, significant progress has been achieved by utilizing both naturally occurring and synthesized variants of MnO_2 , including those prepared via electrochemical (EMD), chemical (CMD), and heat treatment (HTMD) methods [14,15].

Current research focuses mainly on the potential uses of synthetic manganese oxides in various battery cell configurations, either as cathode or anode materials. On the contrary, in the present paper, we examine the electrochemical performance of natural manganese oxides from the manganese ore deposit of Drama area, Greece. The greater area of Drama County was, in the past (1950–1994), the main mining center of Greece for manganese oxide ore, especially of battery-grade quality. Due to extensive mining and ore processing, there are voluminous abandoned mine tailings, low-grade ore, and heaps of ore concentrate at the main mines (25th Km and Mavro Xylo) adjacent to Kato Nevrokopi area, which seek environmental management [16]. Manganese ore ranks among the most extensively processed materials globally, holding crucial significance mainly in the manufacturing of steel alloys, chemicals, and batteries [17]. Nevertheless, the mining processing of this ore results in the accumulation of substantial waste in open-air landfills, with a high environmental impact, contaminating the soil and plants but, most importantly, affecting human neural health [18,19]. Hence, this paper also explores the valorization potential of manganese oxide mining wastes. Manganese ore tailings have been studied extensively through the years, revealing various applications, such as the recovery of soluble manganese and their use in ceramic materials [20,21]. However, one of the most optimal exploitations is their use as cathode material for zinc ion batteries [22]. This study endeavors to discover an even more cost-effective and simplified approach to harnessing these tailings, as well as aiding the transition to green energy.

2. Materials and Methods

2.1. Sample Selection

The samples collected represent ore from waste piles which are disposed of adjacent to the closed mine sites of Mavro Xylo and “25th Km”, Kato Nevrokopi, Drama, Greece. The ore paragenesis in these sites mainly consists of pyrolusite, nsutite (MnO_2), and todorokite [$\text{Ca,K,Na,Mg,Ba,Mn}(\text{Mn,Mg,Al})_6\text{O}_{12} \cdot 3\text{H}_2\text{O}$] at various abundances [23,24]. The mineralogy of the studied samples is verified prior to the experiments by XRD analysis showing that the MLX3 is mostly comprised of nsutite and sample MLX1 is a mixture of nsutite and todorokite with minor matrix calcite. Therefore, the selected samples are representative of the typical waste ore in the area of interest.

2.2. Mineralogical Characterization

Mineralogical analysis was conducted by X-ray diffraction (Bruker D8 ADVANCE, Bruker Corporation, Billerica, MA, USA). XRD patterns were collected among 2θ angles of $5\text{--}75^\circ$ (at Cu $K\alpha$ radiation of 40 kV, 25 mA, and $\lambda = 1.5406 \text{ \AA}$). Mineral phases were identified using the Joint Committee for Power Diffraction Standards (JCPDS) file and the software of DIFFRAC.EVA (V6.1, Bruker Corporation, Billerica, MA, USA) provided by Bruker. The crystallite size of the powders was calculated from the broadening of the Bragg reflections with the application of the Debye–Scherrer equation (Equation (1)) [25]. The samples were also analyzed with transmission electron microscopy (Jeol 2100 HR, Tokyo,

Japan, 200 kV). Elemental analyses were carried out using an Oxford X-Max 100 Silicon Drift Energy Dispersive X-ray spectrometer (EDS) connected to TEM.

In 1918, P. Scherrer described the phenomenon of a beam's expansion when parallel monochromatic radiation falls on a randomly oriented mass of crystals due to the small size of the crystallite [26,27].

$$D = \frac{K \times \lambda}{\beta \times \cos\theta} \quad (1)$$

where D is the size of the crystallite (nm), K is known as the Scherer's constant ($K = 0.89$), λ is the X-ray wavelength (1.5406 Å), β is full width at half maximum (FWHM) of the diffraction peak, and θ ($^\circ$) is the angle of diffraction.

Moreover, specifically for γ - MnO_2 , the percentage of micro-twinning and the de Wolff defect were quantified by using the equations of Chabre and Pannetier (Equation (2)) and P.M. De Wolff (Equation (3)) [12,13].

$$Tw(\text{in}\%) = 100 - 25.20 \Delta 2\theta \quad [\text{for reflections } 002 \text{ and } 061, \text{ CuK}\alpha \text{ radiation}] \quad (2)$$

where $Tw = 0\%$ equals a defectless ramsdellite structure.

$$P_r = 0.602 \times \delta(\text{DW}) - 0.198 \times \delta^2(\text{DW}) + 0.026 \times \delta^3(\text{DW}) \quad (3)$$

where $\delta(\text{DW}) = 2\theta 100_{exp} - \delta(Tw) - 21.808$ (in degrees 2θ)

When $Tw < 55\%$, $\delta(Tw) = -0.0054 \times Tw - 8.9 \times 10^{-5} \times Tw^2$.

When $Tw > 55\%$, $\delta(Tw) = -0.56$.

where $0 \leq P_r \leq 1$, 0 being the ideal ramsdellite structure with no intergrowth of pyrolusite 1×1 tunnels and 1 being the rutile-like structure of pyrolusite.

Since nsutite (γ - MnO_2), as a natural manganese oxide, might not be a homogenous material, thus affecting the electrochemical properties. An investigation was carried out to find an additional route. Recent studies have directed their attention toward different manganese oxides to identify a fitting contender for electrochemical capacitors. Within this group of oxides, hausmannite (Mn_3O_4) stands out as a potential electrode material for supercapacitors due to its numerous advantages compared to alternative solutions. It is the most stable phase of manganese oxide, exhibiting strong redox capabilities and high theoretical specific capacitance [28].

In 1948, McMurdie and Golovato studied the modifications of Manganese oxides at different temperatures [29]. Following their work, Bish and Post studied the behavior under thermal treatment of the complex, tunneled-structured manganese oxides [30]. Both concluded that all of the different phases of manganese oxides transform to Mn_3O_4 at temperatures over 700–800 °C. Therefore, as part of this investigation, the specimens underwent heat treatment using a chamber furnace (Carbolite CWF 1200) at a temperature of 1000 °C for two hours to assess the thermal changes in our samples and their possible transition into hausmannite which was utilized as an electrode in the electrochemical experiments.

2.3. Electrochemical Characterization

Both nsutite (MXL3) and hausmannite (MXL3HT) powders were used separately for the electrode preparations. These electrodes were prepared by combining hausmannite (or nsutite) and carbon black (Merck) with a binder mixture containing poly(vinylidene) fluoride ($-\text{CH}_2\text{CF}_2-$) and 1-methyl-2-pyrrolidone ($\text{C}_5\text{H}_9\text{NO}$). The solid components, which included mineral powder, carbon black, and poly(vinylidene) fluoride, were mixed in a ratio of 7:2:1, while the ratio of mineral powder to solvent ($\text{C}_5\text{H}_9\text{NO}$) was 70 mg:1.4 g [31]. The mixture was subjected to 30 min of sonication and was then deposited onto carbon paper (Toray carbon black, TGP-H-60, Thermo Scientific, Waltham, MA, USA) measuring $1 \text{ cm} \times 1 \text{ cm}$. Subsequently, it was dried in a dry oven for approximately 12 h at 80 °C. The electrode area mass loading was 1.2 mg/cm² for hausmannite and 4.3 mg/cm² for nsutite.

A VersaSTAT 3 Potentiostat Galvanostat (AMETEK, Inc., Berwyn, Pennsylvania, USA) and the VersaSTAT software (version 2.63.3.0) were used for the cyclic voltammetry (CV) and charge–discharge (CDC) measurements. The measurements were extracted using a three-electrode single-compartment cell, including an Ag/AgCl electrode (reference electrode), a Pt wire (counter-electrode), and the prepared materials of hausmannite and nsutite (working electrodes) at room temperature under Ar conditions (Figure 1).

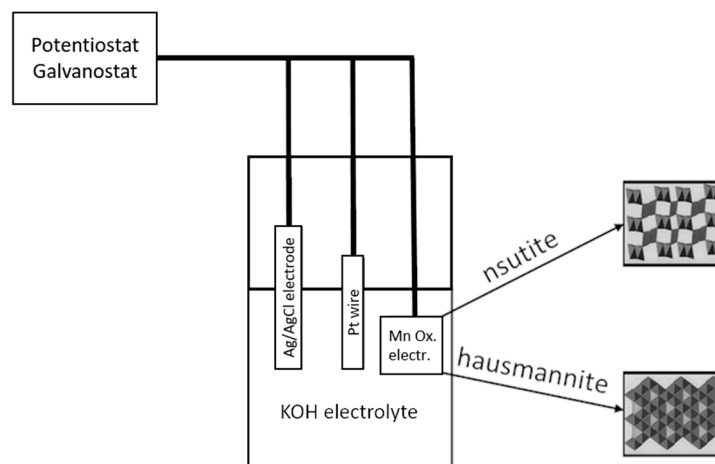


Figure 1. Graphical representation of the three-electrode setup used for the electrochemical characterization of the two manganese oxide electrodes.

The electrochemical properties of these working electrodes were examined in 0.1 M Potassium Hydroxide, KOH, supporting electrolyte solution. (Potassium Hydroxide Pellets, Merck (Sigma-Aldrich, Saint Louis, MO, USA). All the potentials reported for the cyclic voltammetry measurements are expressed vs. NHE after correction.

The electrodes' electrochemical properties, such as specific capacitance (F/g), energy density (Wh/Kg), and power density (W/Kg), were calculated from cyclic voltammetry and charge–discharge measurements using the following equations [32,33]

$$C_p = \frac{Q}{\Delta V} = \frac{(I \times t)}{\Delta V} \quad (4)$$

where C_p (F/g), Q (C), I (A/g), t (s), and ΔV (V) are the specific capacitance, charge, specific current, discharge time, and potential window, respectively.

$$E = \frac{(C_p \times \Delta V^2)}{2} \quad (5)$$

where E (Wh/Kg), C_p (F/g), and ΔV (V) are the energy density, specific capacitance, and potential window, respectively.

$$P = \frac{E}{\Delta t} \quad (6)$$

where P (W/Kg), E (Wh/Kg), and Δt (hr) are the power density, energy density, and discharge time, respectively.

Then, the calculations based on Equations (5) and (6) were graphed on a Ragone plot. This plot was used to compare the energy density and power density across different energy-storage systems to find the best-fitting application of our electrodes [34,35].

3. Results and Discussion

3.1. X-ray Diffraction Analysis

A structural analysis of the samples was carried out using pXRD and is given in Figure 1 and Table 1. The XRD of MXL1 (Figure 2a) shows a predominant peak at a 2θ

value of 29.5° which, together with the peaks at 23.1° , 36° , 39.4° , 43.16° , 47.13° , 47.51° , 48.51° , corresponds to the mineral phase of calcite (CaCO_3). Apart from calcite, strong peaks appear at 2θ values of 9.23° , 12.2° , 18.2° , 37.52° , and 60.28° , which are attributed to the crystal planes of todorokite. Lastly, the 2θ values of 22.14° , 34.75° , 36.86° , 38.8° , 40.36° , 42.26° , 43.3° , 55.95° , 56.66° , and 62.59° were attributed to the mineral phase of nsutite [6,36–38].

Table 1. XRD data for the nsutite, todorokite, and calcite together with the miller indices (hkl).

Nsutite [13]		Todorokite [37]		Calcite [38]	
2θ	<i>hkl</i>	2θ	<i>hkl</i>	2θ	<i>hkl</i>
22.14	110	9.23	100	23.1	012
34.75	130	12.2	110	36	110
36.86	021	18.2	200	39.4	113
38.8	040	18.55	120	43.16	202
40.36	200	26.21	300	47.13	024
42.26	121	37.52	201	47.51	018
43.3	140	41.23	031	48.51	116
55.95	221	49.86	440		
56.66	240	60.28	521		

Powders from sample MXL3 gave similar peaks (Figure 2b), which resemble the pattern of the mineral phase of nsutite but with some of their peaks shifted [39]. The alterations of the 2θ values are due to the aforementioned structural defects (micro-twinning, De Wolff defect) of $\gamma\text{-MnO}_2$. Despite having many similarities, recent studies indicate a high degree of structural heterogeneity among $\gamma\text{-MnO}_2$; therefore, for the specimens from Kato Nevrokopi (Drama, Greece), an attempt was made to calculate these structural defects.

According to the research of Chabre and Pannetier (1995) [13], the intensity profile of $\gamma\text{-MnO}_2$ diffraction patterns is governed by two kinds of defects that modify both the position and shape of most diffraction lines:

- The more or less random stacking of the ramsdellite and pyrolusite structures;
- The micro-twinning of the ramsdellite lattice in 021/061 planes.

For example, if the 2θ peak of 21.8° (1 1 0) is shifted to lower 2θ values, that is a consequence of the micro-twinning of the structure. On the other hand, if the same peak is shifted to higher values, then that is due to De Wolff disorder.

As a result, the powder diffraction patterns of manganese dioxides should be analyzed carefully. The line shifts due to micro-twinning and De Wolff defect are given in Table 2, alongside the line positions of our samples compared to those of a defectless ramsdellite.

Table 2. Shift of 2theta positions due to micro-twinning and De Wolff disorder on sample MXL3.

Miller Indices			Ideal Ramsdellite	MXL3			
<i>h</i>	<i>k</i>	<i>l</i>	2θ (CuKa)	2θ (CuKa) Measured	$\Delta 2\theta$ Ideal	Micro-Twinning	De Wolff
1	1	0	21.8	22.14	0.34	–	+
1	3	0	35.1	34.75	–0.35	+	–
0	2	1	36.8	36.86	0.06	+	
1	1	1	38.4	–		–	–
0	4	0	38.8	38.4	–0.4	–	

Table 2. Cont.

Miller Indices			Ideal Ramsdellite	MXL3			
h	k	l	2θ (CuKa)	2θ (CuKa) Measured	Δ2θ Ideal	Micro-Twinning	De Wolff
2	0	0	39.7	40.36	0.66		
1	2	1	42	42.26	0.26	+	
1	4	0	43.8	43.3	−0.5	−	
1	3	1	47.7	47.933	0.233	−	+
2	2	1	55.3	55.95	0.65	+	
2	4	0	56.8	56.66	−0.14	−	
2	3	1	60	−	−	−	+
1	5	1	63.1	62.59	−0.51	+	−
0	0	2	65	66.035	1.035	+	
0	6	1	69	68.09	−0.91	−	
3	3	0	69.2	68.73	−0.47	+	−
1	1	2	69.5	69.76	0.26	−	+
3	0	1	70.4	−	−	−	
3	1	1	71.2	−	−	−	−

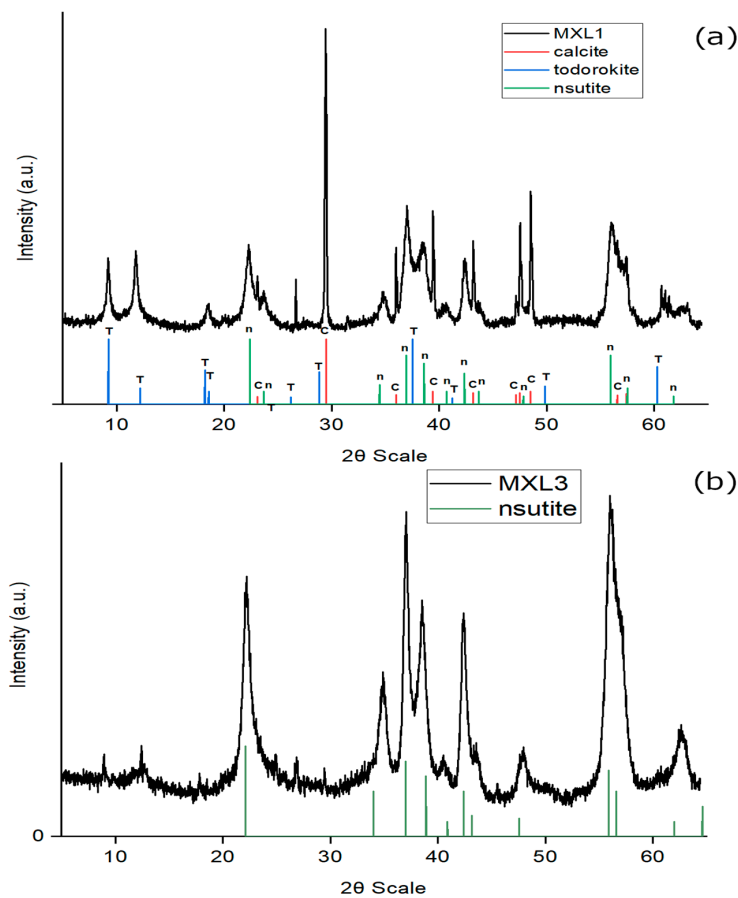


Figure 2. XRD patterns of the samples (a) MXL1 and (b) MXL3, alongside the standard XRD patterns from the identified minerals (intensity in arbitrary units—a.u.).

Micro-twinning (Tw):

Based on the powder diffraction patterns analysis, it has been determined that both defects are present in the samples. The defects were quantified by applying the abovementioned Equations (2) and (3).

$$Tw(in\%) = 100 - 25.20 \Delta 2\theta \quad [for \text{ reflections } 002 \text{ and } 061, \text{ CuK}\alpha \text{ radiation}]$$

$$Tw_{MLX3a} = 51.36\%$$

De Wolff disorder:

$$Pr = 0.602 \times \delta(DW) - 0.198 \times \delta^2(DW) + 0.026 \times \delta^3(DW)$$

$$Pr = 0.42$$

After calculating these parameters, we can project them in a structural diagram (Figure 3) [13] where the following apply:

- A (0,0) is the ideal-defectless ramsdellite;
- B (1,0) represents the pyrolusite;
- C (0,100) describes the fully twinned structure of ramsdellite;
- D (100,0) represents the fully twinned pyrolusite.

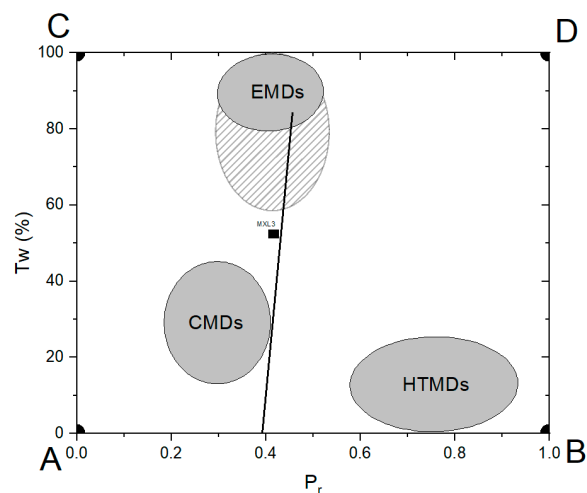


Figure 3. Structural diagram of γ -manganese dioxides. EMDs: Electrochemical Manganese Dioxide, CMDs: Chemical Manganese Dioxide, HTMDs: High-Temperature Manganese Dioxide.

By projecting quantified disorders in this plot from several γ -MnO₂ samples, which included chemically and electrochemically made manganese dioxides (CMD and EMD, respectively), the researchers observed that EMDs, which are widely known for their battery applications, have analog structures [13]. The percentage of micro-twinning is mainly above 60%; as for the Pr value, it seems that EMD samples tend to group along a vertical line at $0.40 \leq Pr \leq 0.45$ values.

Within the diagram (Figure 3), the grey circles depict the standard structural attributes corresponding to each γ -manganese dioxide category. The line-shaded area corresponds to the field of structural imperfections observed in Electrochemical Manganese Dioxides. These measurements were conducted on different EMDs by Chabre and Pannetier [13], defining the extent of structural defects. The black square represents the sample of MXL3, which has structural characteristics similar to the EMDs. Comparing these data to ours, it can be presumed that their structure is very close to those of EMDs and that they are acceptable candidates for dry-cell batteries and supercapacitor applications.

Another characteristic that can be determined from the powder X-ray diffraction pattern is the size of the crystallite of the manganese oxides. By calculating the broadening of the Bragg reflection for the characteristic peak (highest intensity peak) of the mineral

phase with the application of the Debye–Scherrer equation (Equation (1)), it is possible to determine the crystallite size *D* (Table 3) [40,41].

Table 3. The calculated crystallite sizes (Equation (1)) of the different mineral phases that are present in the ore samples.

Sample Name	Mineral Phase	D-Crystallite Size (nm)
MXL1	Todorokite	25
MXL3	Nsutite (γ -MnO ₂)	11

These calculations show that the samples of nsutite have very small crystallite sizes that can help elevate their electrochemical properties.

X-ray diffraction analysis was carried out after the heat treatment of both samples (Figure 4). The results indicated that the sample containing only nsutite (MXL3) successfully transformed into a well-crystallized hausmannite (Figure 4a) [39]. In contrast, the MXL1 sample (Figure 4b) transitioned not only into hausmannite but also into mineral phases like braunite ([Mn²⁺Mn³⁺]₆[SiO₄]₈), tephroite ([Mn²⁺]₂SiO₄), and Manganosite (MnO). This occurrence is likely due to the presence of manganese oxides (todorokite and nsutite) in conjunction with calcite (CaCO₃) and quartz (SiO₂) in the specific sample, which may act as catalysts in the development of manganese silicates, meaning the samples of manganese oxides that contain matrix calcite and quartz need to be separated first and then undergo heat treatment in order to transform into hausmannite successfully.

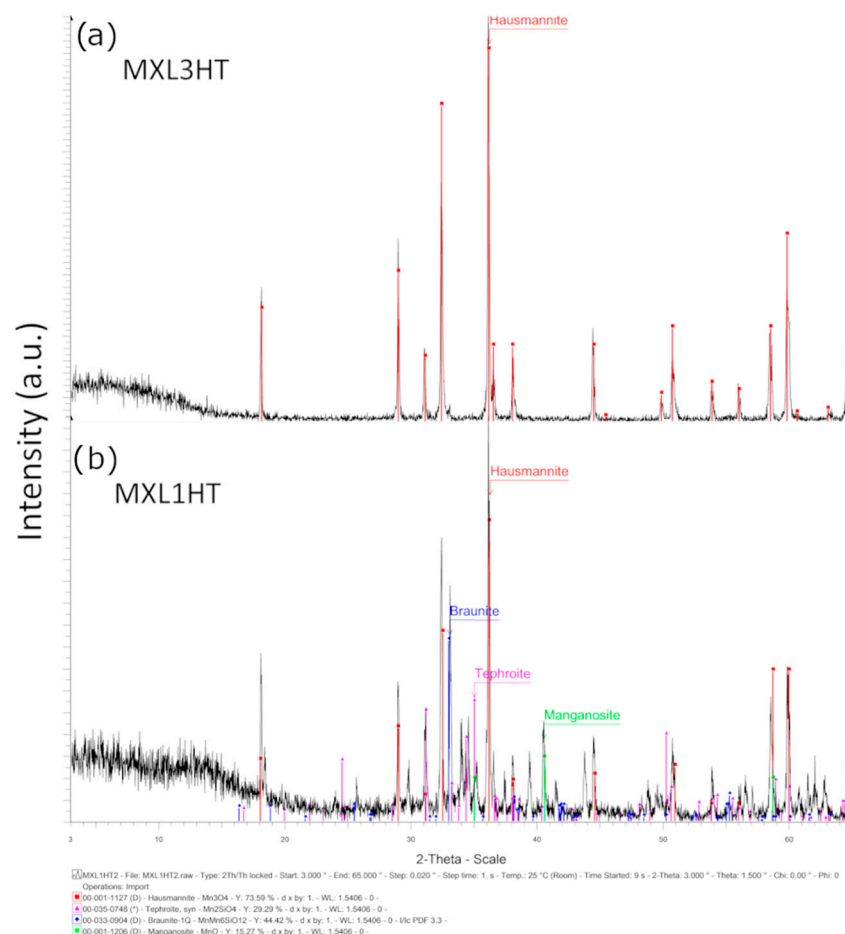


Figure 4. X-ray diffraction patterns of (a) MXL3 and (b) MXL1 after the heat treatment at 1000 °C for two hours (intensity in arbitrary units—a.u.).

3.2. Transmission Electron Microscope Analysis

The samples of MLX3 have been analyzed by an Transmission Electron Microscope to verify and characterize the structure of nsutite (Figure 5). TEM results and the selected area electron diffraction patterns (Table 4) confirm that the structure of the mineral is that of nsutite; even so, the X-ray energy dispersive spectra (EDS) indicate that, although the structure of nsutite is present, its chemical composition resembles that of todorokite (Table S1) [42]. The process of hydrothermal fluid alteration can explain this phenomenon. It has been reported by Thackeray (1997) that when a manganese oxide with a structure of α - MnO_2 (hollandite, todorokite, etc.) comes in contact with a low-pH fluid for prolonged periods, the primarily formed α - MnO_2 converts to a ramsdellite- MnO_2 structure [5]. In this case, todorokite was the first mineral that occurred with a chemical formula of $[\text{Ca}, \text{K}, \text{Na}, \text{Mg}, \text{Ba}, \text{Mn}](\text{Mn}, \text{Mg}, \text{Al})_6\text{O}_{12} \cdot 3\text{H}_2\text{O}$, and after the process of hydrothermal alteration, nsutite was formed. This is also confirmed by the impurities of sulfur (S), zinc (Zn), and lead (Pb) in the mineral phase of nsutite (Table S1). Additionally, different phases of manganese oxide formed on a nanoscale, with a high Pb concentration, which probably represents coronadite $[\text{Pb}(\text{Mn}^{4+}, \text{Mn}^{2+})_8\text{O}_{16}]$.

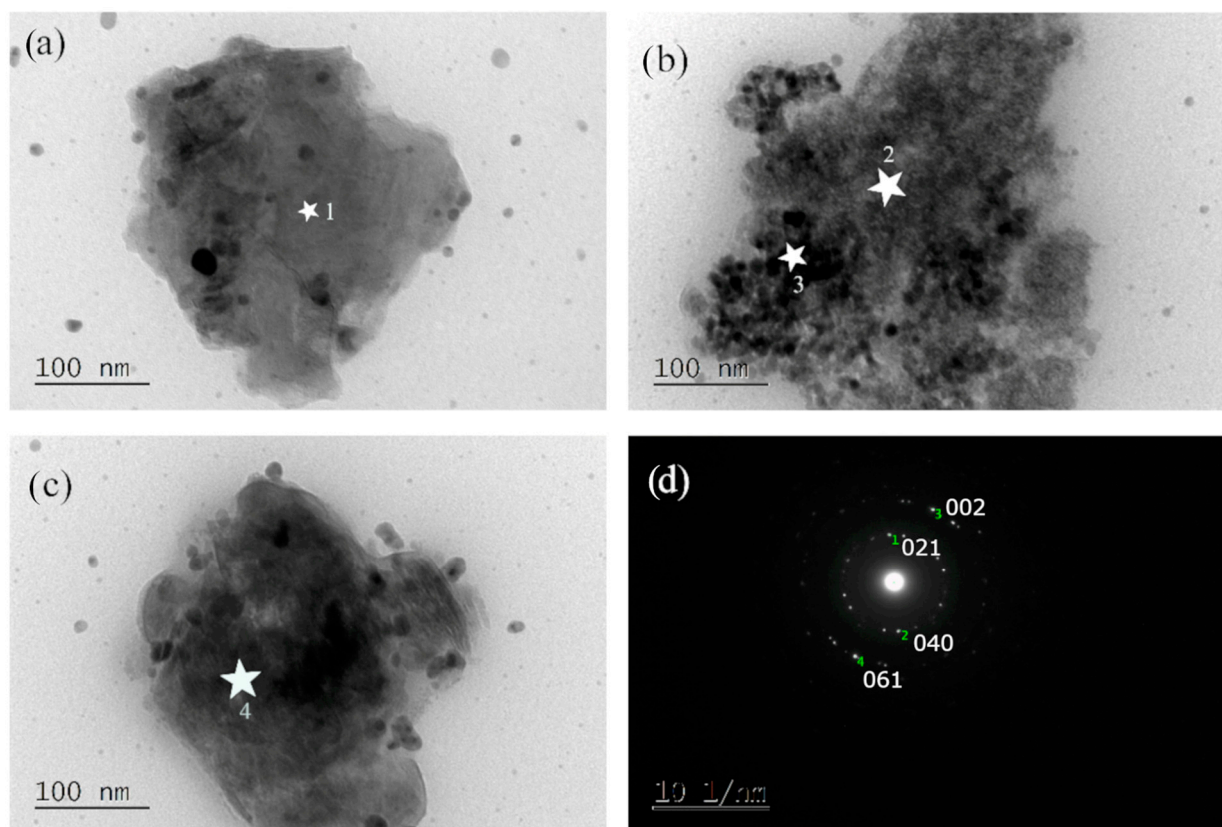


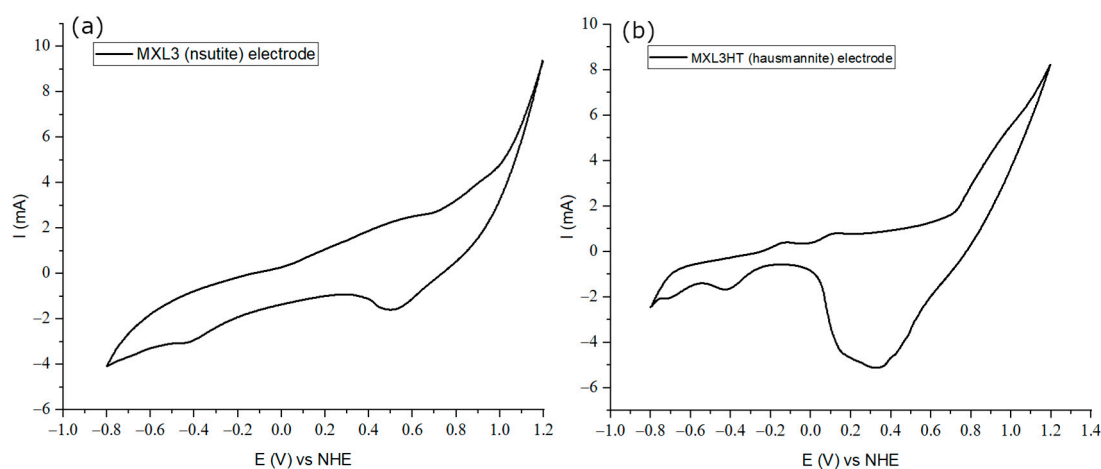
Figure 5. TEM images of manganese oxides from the sample of MLX3c. (a–c) are different grains of the MLX3 sample, and (d) is a selected area electron diffraction pattern of (a) that shows the d spacing of the selected grain. Star-shaped symbols indicate where the energy dispersive spectra was taken. In all the images, two different phases of manganese oxides are present: dark grey represents the phase of nsutite, and dark spheroids represent the mineral phase of coronadite.

Table 4. Selected area electron diffraction patterns solution and its correlation with corresponding d spacing calculated from powder X-ray diffraction (pXRD) signify nsutite’s structural characteristics.

	d Spacing Calculated from SAED (nm)	d Spacing Calculated from pXRD (nm)	Hkl Lattices	2theta Peak (pXRD)
1	0.2396	0.2336	0 2 1	36.89
2	0.2424	0.2434	0 4 0	38.4
3	0.1385	0.1375	0 0 2	66.035
4	0.1404	0.1413	0 6 1	68.09

3.3. Electrochemical Experiments

Cyclic voltammetry and charge–discharge tests were conducted to characterize the electrochemical performance of nsutite and hausmannite composites. Figure 6 shows the cyclic voltammograms of MXL3 (nsutite) and MXL3HT (hausmannite) electrodes with a scan rate of 50 mV/s in a potential window of (−0.8, 1.2) and (−0.8, 1.2), respectively, using as reference electrode Ag/AgCl and Pt as the counter electrode. The two electrodes show a noticeable deviation from each other due to the different nature of the material. Apropos the cyclic voltammetry, experiments were carried out to investigate the redox processes at the electrodes. In MXL3 and MXL3HT voltammograms, the anodic peaks of +0.83 V (MXL3) and +0.85 (MLX3HT) and the cathodic peaks of +0.48 V (MXL3) and +0.35 V (MXL3HT) correspond to the oxygen evolution (OER) and oxygen reduction (ORR) reactions [40].

**Figure 6.** Cyclic voltammograms of (a) MXL3 (nsutite) and (b) MXL3HT (hausmannite) in a 0.1 M KOH electrolyte at a scan rate of 50 mV/s and potential window of [−0.8, 1.2] and [−0.8, 1.2], respectively.

The oxygen evolution reaction (OER) and oxygen reduction reaction (ORR) are two important processes that occur in electrochemical systems, particularly in fuel cells and metal–air batteries. The oxygen evolution reaction is a key process in electrochemical water splitting or electrolysis, where water is split into oxygen and hydrogen gas and usually occurs at the anode electrode of an electrochemical cell. The oxygen reduction reaction is an important process in energy conversion devices such as fuel cells and metal–air batteries, which involves the reduction of oxygen molecules from the air, usually to water, by accepting electrons and protons. The ORR typically occurs at the cathode electrode of an electrochemical cell [43].

Both voltammograms’ remaining anodic and cathodic peaks correlate with the manganese redox reactions. The cathodic peaks correspond to the reduction of the manganese

oxidation state, while the anodic peaks correspond to the oxidation of the manganese oxidation state [44–46].

Charge–discharge (CDC) experiments can provide helpful information about the electrochemical characteristics of the electrodes and their capabilities in energy-storage applications. For the CDC tests (Figure 7), three different current densities (A/g) were used for each electrode, which was calculated by dividing the constant current of the experiments (0.2 mA, 2 mA, 200 mA) with the active mass of the electrodes (4.3 mg for nsutite and 1.2 mg for hausmannite). Current densities were more elevated in the MXL3HT electrode, leading to its superior performance compared to the MXL3 electrode. This difference can be traced back to the non-uniform nature of the MXL3 sample in contrast to the homogeneity achieved through the heat treatment in the case of hausmannite.

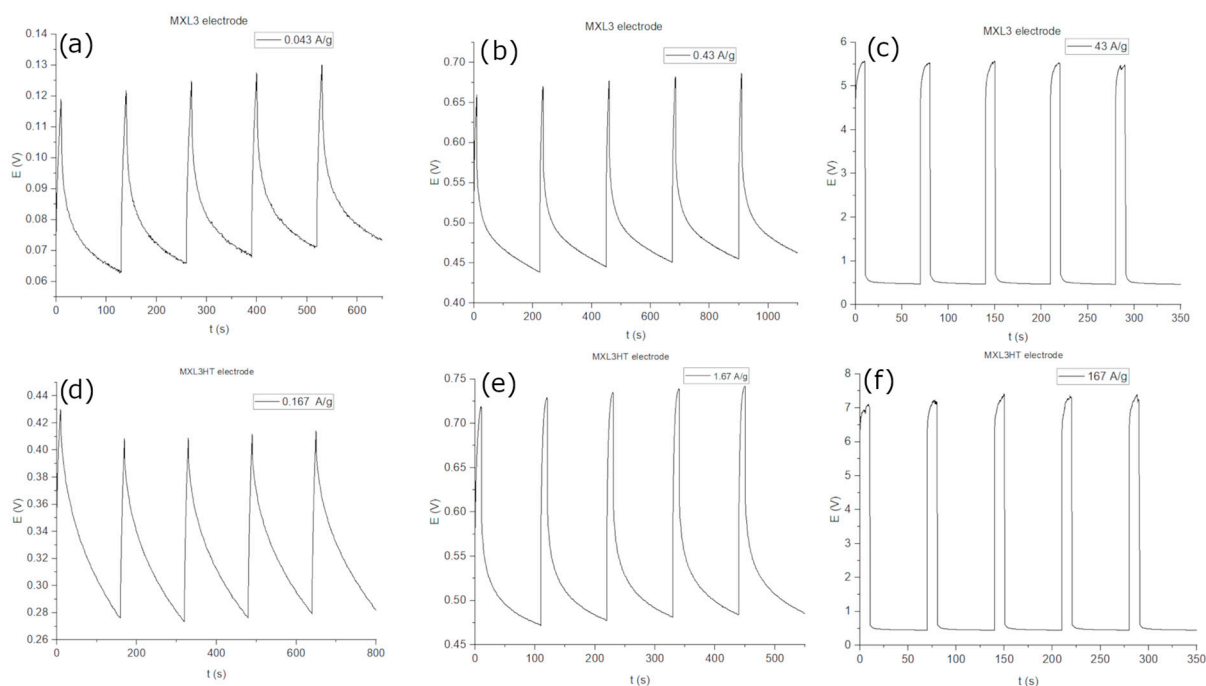


Figure 7. Charge–discharge diagrams of sample MXL3 (a–c) and MXL3HT (hausmannite) electrodes (d–f) at a constant current of 0.2 mA, 2 mA, and 200 mA.

Subsequently, the specific capacitance, energy density, and power density of both electrodes were determined using Equations (4)–(6). The results are presented in Table 5.

Table 5. Electrochemical calculations using the abovementioned equations for the MXL3 (nsutite) and MXL3HT (hausmannite) electrodes.

Electrodes	Current Density (A/g)	Specific Capacitance (F/g)	Energy Density (Wh/Kg)	Power Density (W/Kg)
MXL3	0.043	92.55	0.04	1.27
	0.43	434.8	2.79	46.77
	43	17.39	60.38	107,684
MXL3HT	0.167	191	0.45	10.82
	1.67	667.3	5.93	213.78
	167	38.65	234.5	551,765

The energy and power densities were then graphed on a Ragone plot (Figure 8) to identify the most suitable application for these electrodes [47].

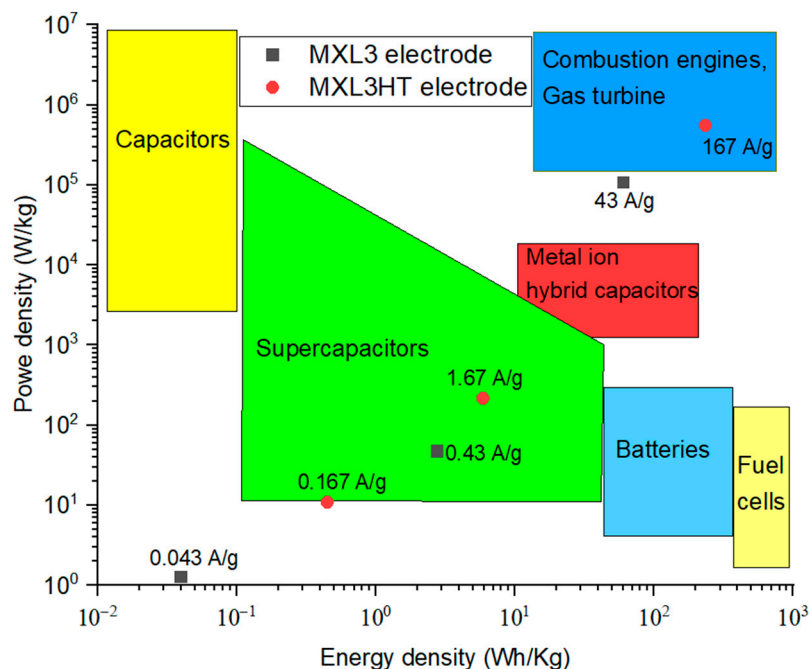


Figure 8. Ragone plot representing various energy storage systems, along with the computations for the MXL3 (nsutite) and MXL3HT (hausmannite) electrode characteristics.

The Ragone plot shows that the hausmannite-based electrode exhibits a higher potential to function effectively as a supercapacitor than the nsutite counterpart. The nsutite electrode also holds supercapacitor potential, albeit under certain limited conditions. This probably arises from the heterogeneity of the natural manganese oxides, as observed with the TEM analysis. Moreover, the hausmannite electrode (MXL3HT) shares attributes comparable to a combustion engine, implying its ability to deliver substantial power output within a brief timeframe. Two additional hausmannite electrodes were created and subjected to identical electrochemical experiments, which confirmed these findings.

The cyclic stability of the MXL3HT electrode was analyzed by performing a 1000-cycle charge–discharge test at a current density of 167 A/g (Figure S1) [48]. The capacitance retention shows no noteworthy alteration, indicating the necessity for additional examination with even longer cycles to observe the electrode’s maximum cycle count.

Many studies have shown that pure and synthetic nsutite (or γ -MnO₂) is the best candidate among the manganese oxides for energy applications [10,11]. Nsutite’s high electrochemical performance correlates with its structure and the presence of Mn⁴⁺, while hausmannite’s spinel-like structure and the presence of Mn²⁺ and Mn³⁺ make it an inferior choice [49]. However, in this study, nsutite is not a homogenous material (Figure 5), while hausmannite, as shown in Figure 4, is well-crystallized due to heat treatment. Hence, hausmannite emerges as the optimal choice for repurposing waste ores in energy storage applications, not only due to its superior performance but also owing to its potential for greater abundance compared to nsutite. This is because all manganese oxides can convert into hausmannite through heat treatment [29,30].

4. Conclusions

This research highlights the structural and electrochemical characteristics of certain manganese oxides found in the waste piles of abandoned mines located at Mavro Xylo in the Drama region, Greece. Although the chemical composition resembles the manganese oxide phase of todorokite, nsutite emerges as the sample’s dominant phase due to hydrothermal alterations in the area of interest. Even though nsutite (γ -MnO₂) is one of the most promising candidates for energy applications, the samples’ heterogeneity necessitates exploring an alternative approach in this particular case. Therefore, hausmannite was

produced by subjecting nsutite and todorokite samples to heat treatment in a dry oven. Two separate electrodes were created, utilizing nsutite and hausmannite as the primary components. The results of electrochemical experiments on these electrodes suggest that further investigation into the structural aspects of hausmannite is a promising avenue. Furthermore, they suggest that the mining wastes located in Greece and around the world can hopefully be utilized to manufacture energy storage electrodes, which can bring economic and environmental benefits in view of their valorization and could support the swift towards green energy.

Supplementary Materials: The following supporting information can be downloaded at: <https://www.mdpi.com/article/10.3390/min14050455/s1>, Figure S1: Cycle performance of hausmannite electrode (MXL3HT), Table S1: Elemental composition obtained by TEM/EDS for sample MXL3.

Author Contributions: Methodology, G.S. and M.K.; software, G.S. and M.K.; validation, G.S., M.K., C.S. and C.A.M.; formal analysis, G.S. and M.K.; investigation, G.S. and M.K.; resources, G.S., M.K. and C.A.M.; data curation, G.S. and M.K.; writing—original draft preparation, G.S. and M.K.; writing—review and editing, M.K., C.S. and C.A.M.; visualization, G.S., M.K., C.S. and C.A.M.; supervision, G.S., C.S. and C.A.M.; All authors have read and agreed to the published version of the manuscript.

Funding: The Hellenic Foundation for Research and Innovation (HFRI) supported G.S.'s research under the 4th Call for HFRI PhD Fellowships (Fellowship Number: 11210).

Data Availability Statement: Data are contained within the article and Supplementary Materials.

Acknowledgments: All powder diffraction data were collected in the National and Kapodistrian University of Athens X-ray diffraction Core Facility by Panagiotis Tzevelekidis. All Transmission Electron Microscope data were collected in the School of Mining and Metallurgical Engineering, National Technical University of Athens, by Petros Tsakiridis.

Conflicts of Interest: The authors declare no conflicts of interest.

References

1. Ghosh, S.K. Diversity in the Family of Manganese Oxides at the Nanoscale: From Fundamentals to Applications. *ACS Omega* **2020**, *5*, 25493–25504. [CrossRef]
2. Yang, X.; Peng, Q.; Liu, L.; Tan, W.; Qiu, G.; Liu, C.; Dang, Z. Synergistic Adsorption of Cd(II) and As(V) on Birnessite under Electrochemical Control. *Chemosphere* **2020**, *247*, 125822. [CrossRef]
3. Rout, K.; Mohapatra, M.; Mohapatra, B.K.; Anand, S. Pb(II), Cd(II) and Zn(II) Adsorption on Low Grade Manganese Ore. *Int. J. Eng. Sci. Technol.* **2009**, *1*, 106–122. [CrossRef]
4. Radinger, H.; Connor, P.; Stark, R.; Jaegermann, W.; Kaiser, B. Manganese Oxide as an Inorganic Catalyst for the Oxygen Evolution Reaction Studied by X-ray Photoelectron and Operando Raman Spectroscopy. *ChemCatChem* **2021**, *13*, 1175–1185. [CrossRef]
5. Thackeray, M.M. Manganese Oxides for Lithium Batteries. *Prog. Solid State Chem.* **1997**, *25*, 1–71. [CrossRef]
6. Choudhary, N.; Li, C.; Moore, J.; Nagaiah, N.; Zhai, L.; Jung, Y.; Thomas, J. Asymmetric supercapacitor electrodes and devices. *Adv. Mater.* **2017**, *29*, 1605336. [CrossRef]
7. Post, J.E. Manganese Oxide Minerals: Crystal Structures and Economic and Environmental Significance. *Proc. Natl. Acad. Sci. USA* **1999**, *96*, 3447–3454. [CrossRef]
8. Post, J.E.; McKeown, D.A.; Heaney, P.J. Raman Spectroscopy Study of Manganese Oxides: Tunnel Structures. *Am. Miner.* **2020**, *105*, 1175–1190. [CrossRef]
9. Post, J.E.; McKeown, D.A.; Heaney, P.J. Raman Spectroscopy Study of Manganese Oxides: Layer Structures. *Am. Miner.* **2021**, *106*, 351–366. [CrossRef]
10. Kondo, T.; Matsushima, Y.; Matsuda, K.; Unuma, H. Electrochemical Properties of δ - and γ -MnO₂ Thin Films Deposited by a Chemical Bath Technique. *J. Mater. Sci. Mater. Electron.* **2016**, *27*, 8001–8005. [CrossRef]
11. Magnard, N.P.L.; Anker, A.S.; Aalling-Frederiksen, O.; Kirsch, A.; Jensen, K.M. Characterisation of Intergrowth in Metal Oxide Materials Using Structure-Mining: The Case of γ -MnO₂. *Dalton Trans.* **2022**, *51*, 17150–17161. [CrossRef]
12. de Wolff, P.M. Interpretation of Some γ -MnO₂ Diffraction Patterns. *Acta Crystallogr.* **1959**, *12*, 341–345. [CrossRef]
13. Chabre, Y.; Pannetier, J. Structural and Electrochemical Properties of the Proton/ γ -MnO₂ System. *Prog. Solid State Chem.* **1995**, *23*, 1–130. [CrossRef]
14. Liu, Y.-Y.; Lv, T.-T.; Wang, H.; Guo, X.-T.; Liu, C.-S.; Pang, H. Nsutite-type VO₂ microcrystals as highly durable cathode materials for aqueous zinc-ion batteries. *Chem. Eng. J.* **2021**, *417*, 128408. [CrossRef]
15. Julien, C.M.; Mauger, A. Nanostructured MnO₂ as Electrode Materials for Energy Storage. *Nanomaterials* **2017**, *7*, 396. [CrossRef]

16. Sofianska, E.; Michailidis, K. Assessment of heavy metals contamination and potential ecological risk in soils affected by a former Mn mining activity, Drama District, Northern Greece. *Soil Sediment Contam. Int. J.* **2016**, *25*, 296–312. [[CrossRef](#)]
17. Gomes-Pimentel, M.; da Silva, M.R.C.; Viveiros, D.d.C.S.; Picanço, M.S. Manganese Mining Waste as a Novel Supplementary Material in Portland Cement. *Mater. Lett.* **2022**, *309*, 131459. [[CrossRef](#)]
18. Rodrigues, J.L.; Araújo, C.F.; dos Santos, N.R.; Bandeira, M.J.; Anjos, A.L.S.; Carvalho, C.F.; Lima, C.S.; Abreu, J.N.S.; Mergler, D.; Menezes-Filho, J.A. Airborne Manganese Exposure and Neurobehavior in School-Aged Children Living near a Ferro-Manganese Alloy Plant. *Environ. Res.* **2018**, *167*, 66–77. [[CrossRef](#)]
19. Rivera-Becerril, F.; Juárez-Vázquez, L.V.; Hernández-Cervantes, S.C.; Acevedo-Sandoval, O.A.; Vela-Correa, G.; Cruz-Chávez, E.; Moreno-Espíndola, I.P.; Esquivel-Herrera, A.; de León-González, F. Impacts of Manganese Mining Activity on the Environment: Interactions Among Soil, Plants, and Arbuscular Mycorrhiza. *Arch. Environ. Contam. Toxicol.* **2013**, *64*, 219–227. [[CrossRef](#)]
20. Troy, P.J.; Wiltshire, J.C. Manganese tailings: Useful properties suggest a potential for gas absorbent and ceramic materials. *Mar. Georesources Geotechnol.* **1998**, *16*, 273–281. [[CrossRef](#)]
21. Santos, O.d.S.H.; Carvalho, C.d.F.; da Silva, G.A.; dos Santos, C.G. Manganese ore tailing: Optimization of acid leaching conditions and recovery of soluble manganese. *J. Environ. Manag.* **2015**, *147*, 314–320. [[CrossRef](#)]
22. Yao, J.; Yu, T.; Huang, Q.; Li, Y.; Huang, B.; Yang, J. Preparation of Mn₂O₃/Fe₂O₃ composite cathode material for zinc ion batteries from the reduction leaching solution of manganese ore tailing. *J. Ind. Eng. Chem.* **2024**, *in press*. [[CrossRef](#)]
23. Michailidis, K.M.; Nicholson, K.; Nimfopoulos, M.K.; Patrick, R.A.D. An EPMA and SEM Study of the Mn-Oxide Mineralization of Kato Nevrokopi, Macedonia, Northern Greece: Controls on Formation of the Mn⁴⁺ Oxides. *Geol. Soc. Lond. Spéc. Publ.* **1997**, *119*, 265–280. [[CrossRef](#)]
24. Nimfopoulos, M. Manganese Mineralization near Kato Nevrokopi, Drama, Greece. Ph.D. Thesis, Geology Department, University of Manchester, Manchester, UK, 1988.
25. Stötzl, C.; Müller, F.; Reinert, F.; Niederdraenk, F.; Barralet, J.; Gbureck, U. Ion Adsorption Behaviour of Hydroxyapatite with Different Crystallinities. *Colloids Surfaces B Biointerfaces* **2009**, *74*, 91–95. [[CrossRef](#)] [[PubMed](#)]
26. Patterson, A.L. The Scherrer Formula for X-Ray Particle Size Determination. *Phys. Rev. B* **1939**, *56*, 978–982. [[CrossRef](#)]
27. Hossain, S.; Mahmud, M.; Bin Mobarak, M.; Sultana, S.; Shaikh, A.A.; Ahmed, S. New Analytical Models for Precise Calculation of Crystallite Size: Application to Synthetic Hydroxyapatite and Natural Eggshell Crystalline Materials. *Chem. Pap.* **2022**, *76*, 7245–7251. [[CrossRef](#)]
28. Kulkarni, S.; Puthusseri, D.; Thakur, S.; Banpurkar, A.; Patil, S. Hausmannite Manganese Oxide Cathodes for Supercapacitors: Surface Wettability and Electrochemical Properties. *Electrochim. Acta* **2017**, *231*, 460–467. [[CrossRef](#)]
29. McMurdie, H.F.; Golovato, E. Study of the Modifications of Manganese Dioxide. *J. Res. Natl. Bur. Stand.* **1948**, *41*, 589. [[CrossRef](#)]
30. Bish, D.L.; Post, J.E. Thermal Behavior of Complex, Tunnel-Structure Manganese Oxides. *Am. Mineral.* **1989**, *74*, 177–186.
31. Stoševski, I.; Bonakdarpour, A.; Fang, B.; Voon, S.T.; Wilkinson, D.P. Hausmannite Mn₃O₄ as a Positive Active Electrode Material for Rechargeable Aqueous Mn-Oxide/Zn Batteries. *Int. J. Energy Res.* **2021**, *45*, 220–230. [[CrossRef](#)]
32. Jiang, H.; Yang, L.; Li, C.; Yan, C.; Lee, P.S.; Ma, J. High-Rate Electrochemical Capacitors from Highly Graphitic Carbon-Tipped Manganese Oxide/Mesoporous Carbon/Manganese Oxide Hybrid Nanowires. *Energy Environ. Sci.* **2011**, *4*, 1813–1819. [[CrossRef](#)]
33. Nguyen, T.; Boudard, M.; Carmezim, M.J.; Montemor, M.F. Layered Ni(OH)₂-Co(OH)₂ Films Prepared by Electrodeposition as Charge Storage Electrodes for Hybrid Supercapacitors. *Sci. Rep.* **2017**, *7*, 39980. [[CrossRef](#)]
34. Simon, P.; Gogotsi, Y. Perspectives for Electrochemical Capacitors and Related Devices. *Nat. Mater.* **2020**, *19*, 1151–1163. [[CrossRef](#)]
35. Lee, S.C.; Jung, W.Y. Analogical Understanding of the Ragone Plot and a New Categorization of Energy Devices. *Energy Procedia* **2016**, *88*, 526–530. [[CrossRef](#)]
36. Singhal, R.; Lembeck, J.; LeMaire, P.C.K., III; Pereira, D.; LeMaire, P. Physical and Electrochemical Characterization of Nsutite. *Am. J. Anal. Chem.* **2021**, *12*, 440–445. [[CrossRef](#)]
37. Faulring, G.M. A study of Cuban Todorokite. *Adv. X-ray Anal.* **1961**, *5*, 117–126. [[CrossRef](#)]
38. Graf, D.L. Crystallographic tables for the rhombohedral carbonates. *Am. Mineral.* **1961**, *46*, 1283–1316.
39. Soulamidis, G.; Stouraiti, C.; Kourmousi, M.; Tzevelekidis, P.; Charalampous, E.; Mitsopoulou, C.A. Structural and Electrochemical Characterization of Natural Manganese Oxides for Energy Storage Applications. *Mater. Proc.* **2023**, *15*, 64. [[CrossRef](#)]
40. Malinger, K.A.; Laubernds, K.; Son, Y.-C.; Suib, S.L. Effects of Microwave Processing on Chemical, Physical, and Catalytic Properties of Todorokite-Type Manganese Oxide. *Chem. Mater.* **2004**, *16*, 4296–4303. [[CrossRef](#)]
41. de Almeida, W.L.; Freisleben, L.C.; Brambilla, B.C.; Isoppo, V.G.; Rodembusch, F.S.; de Sousa, V.C. Influence of Starch Used in the Sol-Gel Synthesis of ZnO Nanopowders. *J. Nanopart. Res.* **2023**, *25*, 75. [[CrossRef](#)]
42. Stouraiti, C.; Lozios, S.; Soukis, K.; Mavrogonatos, C.; Tsikos, H.; Voudouris, P.; Wang, H.; Zamparas, C.; Kollias, K. Manganese Metallogenesis in the Hellenic Arc: Case Studies from a Triassic Rift-Related Volcaniclastic Succession of the Cycladic Blueschist Unit, Greece. *Ore Geol. Rev.* **2022**, *142*, 104694. [[CrossRef](#)]
43. Gowda, C.C.; Mathur, A.; Parui, A.; Kumbhakar, P.; Pandey, P.; Sharma, S.; Chandra, A.; Singh, A.K.; Halder, A.; Tiwary, C.S. Understanding the Electrocatalysis OER and ORR Activity of Ultrathin Spinel Mn₃O₄. *J. Ind. Eng. Chem.* **2022**, *113*, 153–160. [[CrossRef](#)]
44. Chigane, M.; Ishikawa, M. Manganese Oxide Thin Film Preparation by Potentiostatic Electrolyses and Electrochromism. *J. Electrochem. Soc.* **2000**, *147*, 2246. [[CrossRef](#)]

45. Verma, A.; Jha, A.; Basu, S. Manganese Dioxide as a Cathode Catalyst for a Direct Alcohol or Sodium Borohydride Fuel Cell with a Flowing Alkaline Electrolyte. *J. Power Sources* **2005**, *141*, 30–34. [[CrossRef](#)]
46. Rus, E.D.; Moon, G.D.; Bai, J.; Steingart, D.A.; Erdonmez, C.K. Electrochemical Behavior of Electrolytic Manganese Dioxide in Aqueous KOH and LiOH Solutions: A Comparative Study. *J. Electrochem. Soc.* **2015**, *163*, A356. [[CrossRef](#)]
47. Liu, Y.; Wu, Q.; Liu, L.; Manasa, P.; Kang, L.; Ran, F. Vanadium Nitride for Aqueous Supercapacitors: A Topic Review. *J. Mater. Chem. A* **2020**, *8*, 8218–8233. [[CrossRef](#)]
48. Kavitha, E.; Meiyazhagan, S.; Yugeswaran, S.; Balraju, P.; Suresh, K. Electrochemical Prospects and Potential of Hausmannite Mn₃O₄ Nanoparticles Synthesized through Microplasma Discharge for Supercapacitor Applications. *Int. J. Energy Res.* **2021**, *45*, 7038–7056. [[CrossRef](#)]
49. Taguchi, A.; Inoue, S.; Akamaru, S.; Hara, M.; Watanabe, K.; Abe, T. Phase transition and electrochemical capacitance of mechanically treated manganese oxides. *J. Alloys Compd.* **2006**, *414*, 137–141. [[CrossRef](#)]

Disclaimer/Publisher’s Note: The statements, opinions and data contained in all publications are solely those of the individual author(s) and contributor(s) and not of MDPI and/or the editor(s). MDPI and/or the editor(s) disclaim responsibility for any injury to people or property resulting from any ideas, methods, instructions or products referred to in the content.